# Groove Gap-Waveguide Filter with Low-Loss and Dual-Band Capabilities for Satellite IoT Communication Networks Across K-band

Mohammad Alibakhshikenari, Yazeed Mohammad Qasaymeh, Bal Virdee, Chan Hwang See, Yue Ma, Takfarinas Saber, Ernesto Limiti

***Abstract*: This paper presents a dual-band groove gap-waveguide (GGW) filter that provides two separately adjustable passbands within a single-layer structure. The core contribution is a dual-cavity organization that uses two distinct cavity groups operating in the same $TE_{102}$ mode, together with novel I-shaped coupling slots milled in the top plate that serve as the primary mechanism for controlling inter-resonator coupling. This combination provides flexible per-band adjustment of center frequency and bandwidth without resorting to higher-order mode sequencing or multilayer stacks often used in prior GGW implementations, thereby simplifying fabrication and assembly. A prototype addressing space-to-Earth downlink bands exhibits passbands centered at 19.0 and 20.75 GHz, with 3-dB bandwidths of 400 and 280 MHz, respectively, and insertion loss <0.4 dB across both bands. Measured return loss is ≥15 dB, and the contactless GGW realization suppresses parasitic leakage while simplifying machining and assembly. Sensitivity analysis confirms tolerance to typical CNC variations in pin height, air gap, and slot dimensions, supporting reproducible performance. The proposed filter therefore provides a practical RF solution for satellite IoT payloads requiring low loss, spectral agility, and simplified fabrication. Relative to state-of-the-art GGW filters, it achieves a favourable trade-off among complexity, footprint, and electrical performance, facilitating scalable multiband K-band front-ends for emerging satellite IoT networks[1].**

***Keywords*: Groove gap-waveguide (GGW); dual-band filter; cavity resonator; low-loss; satellite IoT communication networks; bandpass filter (BPF); single layer structure; mm-Wave K-band.**

## I. Introduction

RF and microwave transceivers are indispensable in modern wireless communication systems, comprising essential components such as filters [1], [2], antennas [3], diplexers [4], [5], couplers [6], and phase shifters [7]-[9]. These components underpin efficient signal conditioning, transmission, and reception [10]. As operating frequencies increase into the K-band and millimeter wave ranges, conductor and radiation losses intensify and can degrade link budgets if not carefully managed [11], [12]. In response, designers increasingly co-integrate multiple front-end functions to shorten interconnects and mitigate packaging related leakage [13], [14]. This approach reduces complexity, cost, and production time, which makes the solution scalable for high frequency applications such as the K-band.

Gap waveguide technology provides contactless propagation between parallel conducting plates by using an electromagnetic bandgap bed of nails to suppress parallel plate modes [15]. Its variants, namely groove [16], ridge [17], and microstrip ridge [18], enable low loss passive components with relaxed electrical contact requirements. Comprehensive overviews and fabrication options are reported in [19], [20]. Among these, groove gap waveguides (GGWs) [21], [22] are attractive for filters because of their affinity with rectangular waveguides and their dominant $TE_{10}$ behavior, which allows high Q cavities with well controlled inter resonator coupling via apertures or slot perturbations. Practical design targets include low insertion loss, compactness, suppression of spurious modes, and manufacturability.

K- and Ka-bands are prioritized because they provide wider and more contiguous spectrum than L- or S-band, which enables higher aggregate data rates and finer channelization for large IoT populations. The shorter wavelength also allows smaller antennas for a given beamwidth, which supports compact user equipment and dense spot-beam frequency reuse. At the same time, operation at these higher frequencies is more demanding: conductor and interface losses

Co-funded by the European Union. Views and opinions expressed are however those of the author(s) only and do not necessarily reflect those of the European Union or the European Research Executive Agency. Neither the European Union nor the granting authority can be held responsible for them. Besides that, this publication has emanated from research jointly funded by Taighde Éireann – Research Ireland under Grant number 13/RC/2094_2, the European Union's Marie Sklodowska-Curie Actions under grant number 101126578 and was supported in part by University of Galway. *Corresponding Author: Mohammad Alibakhshikenari*.

M. Alibakhshikenari and T. Saber are with the LERO, the Research Ireland Centre for Software, College of Science and Engineering, School of Computer Science, University of Galway, H91 TK33 Galway, Ireland. mohammad.alibakhshikenari@universityofgalway.ie, takfarinas.saber@universityofgalway.ie.
M. Alibakhshikenari is also with the Department of Electrical and Electronics Engineering, Dogus University, 34775 Umraniye, Istanbul, Türkiye.
M. Naser-Moghadasi is with the Computer and Electrical Engineering Department, Science and Research Branch, Islamic Azad University, Tehran 14696-69191, Iran; mn.moghaddasi@srbiau.ac.ir.
B. Virdee is with the Center for Communications Technology, London Metropolitan University, London N7 8DB, United Kingdom; b.virdee@londonmet.ac.uk.
H. Zakeri is with the Department of Electrical Engineering, Amirkabir University of Technology, 15875-4413 Tehran, Iran; h.zakeri@aut.ac.ir.
C. H. See is with the School of Computing, Eng. and the Built Environment, Edinburgh Napier University, Edinburgh, EH10 5DT, U.K.; c.see@napier.ac.uk.
Y. Ma is with the National Astronomical Observatories, Chinese Academy of Sciences, Beijing, 100101, China; yuema@nao.cas.cn.
E. Limiti is with the Electronics Engineering Department, University of Rome "Tor Vergata", 00133 Rome, Italy; limiti@ing.uniroma2.it.

increase, manufacturing tolerances tighten, and atmospheric effects such as rain attenuation are more pronounced near 20–30 GHz. These factors make low insertion loss in front-end filtering especially important. The air-filled GGW approach used here addresses these needs by avoiding bulk dielectric loss, suppressing parallel-plate leakage via the EBG lid, and maintaining a single-layer, contactless structure that reduces ohmic and assembly-related losses in the targeted 19.0 and 20.75 GHz bands.

Positioning with respect to existing GGW filters. Prior GGW bandpass designs often realize single band responses or achieve dual band operation by invoking higher order or sequential modes in a shared cavity, by using multilayer stacks, or by employing dense pin fields that raise machining effort and yield risk, for example [23], [30], [31]. In contrast, this work relies on dual cavity tuning under the same $TE_{102}$ mode but organizes two distinct cavity groups with different physical dimensions and uses I-shaped slots milled in a single top plate to set inter resonator coupling. This arrangement preserves a single-layer structure, enables per band control of center frequency and bandwidth, and targets low insertion loss with simplified fabrication. We refrain from first time claims and instead emphasize these practical distinctions relative to existing GGW dual band filters.

Key design characteristics relative to prior GGW filters.

1. Single-layer dual band GGW architecture uses two $TE_{102}$ cavity groups with distinct dimensions, which enables separate adjustment of each passband's center frequency and bandwidth.
2. I-shaped coupling slots in the top plate that realize strong and selective coupling without multilayer alignment or intricate pin fields, which improves manufacturability.
3. Demonstrated low insertion loss below 0.4 dB at 19.0 and 20.75 GHz with measured return loss of at least 15 dB, which aligns with K-band space to Earth downlink needs while keeping mechanical complexity moderate.

The central contribution of this work is the use of I-shaped coupling slots engraved on the top plate of a single-layer groove gap-waveguide structure to precisely control inter-resonator coupling, enabling separately adjustable dual-band operation with low insertion loss and improved impedance matching.

## II. GGW Bandpass Filter

This section describes the design process for a bandpass filter intended for a space-to-earth satellite communication system operating at 19 and 20.75 GHz. For clarity, the design procedure is presented in three stages aligned with the main contributions of this work. First, the baseline GGW cavity configuration and pin-lattice parameters are established to realize the dual-band resonant behavior. Second, the proposed I-shaped coupling slots are introduced to enhance inter-cavity coupling and achieve the final filter response. Finally, fabrication considerations, tolerance analysis, and experimental validation are presented to demonstrate the practicality of the proposed architecture.

The final proposed filter employs a third-order GGW cavity structure with I-shaped coupling slots engraved on the top plate to enhance inter-cavity coupling and impedance matching. Section II-A presents the baseline cavity synthesis and resonator configuration, while Section II-B introduces the I-shaped coupling mechanism leading to the final optimized filter response.

The two frequency bands are sufficiently separated to prevent interference. The filter is constructed using a GGW, which comprises an array of metal pins protruding from the bottom metallic plate with the top metallic plate positioned above the pins, separated by a narrow air gap. Simply put, in all types of GGWs, the basic structure consists of parallel plates with a magnetic wall and an electrical wall. The magnetic wall is artificially created using an array of λ/4 metal pins. Wave propagation is suppressed in all directions when the distance between the two walls is less than λ/4. A groove in the parallel walls is introduced to create a path for wave propagation. The first step in the design process is determining the parameters of the bed of metal pins to produce the required electromagnetic bandgap stopband. These parameters (pin height $d$, period $p$, pin width $a$, and air gap $g$) were optimized using unit-cell dispersion analysis in CST Microwave Studio to ensure a stopband covering 16–26 GHz. In this design, the electromagnetic bandgap is formed by a rectangular lattice of square pins, as exhibited in Fig.1, with cross-section $a$=1 mm and height $d$=4.25 mm, repeated with period $p$=2 mm along both $x$ and $y$ directions. The top plate is spaced by an air gap of $g$=1 mm above the pin tips, which together with the lattice yields a stopband from 16–26 GHz for parallel-plate modes as depicted in the dispersion diagram. The value of the pin's parameters is stated in Table I, where $\lambda$ is the free-space wavelength at 19 GHz. These optimized dimensions were obtained using CST Microwave Studio, a 3D full-wave electromagnetic (EM) simulation tool.

Despite these systematic steps, challenges often arise. Ensuring no energy leakage due to improper pin array design and achieving precise dimensions during fabrication are common hurdles. By addressing these challenges through careful design, simulation, and testing, a high-performance GGW bandpass filter can be realized. Its bandwidth and center frequency can be controlled by adjusting the cavity dimensions ($g_1$, $g_2$), the inter-cavity spacing ($i$), and the coupling-slot parameters, which determine the resonant frequencies and coupling coefficients of the filter. The periodicity and dimensions of the metallic pins, including their width, height, and spacing, significantly affect the EM field confinement and propagation characteristics, which in turn influence the resonant frequency. Once fabricated, this type of filter is not tunable. Therefore, it is critical to minimize manufacturing tolerances to ensure the design specifications are accurately met.

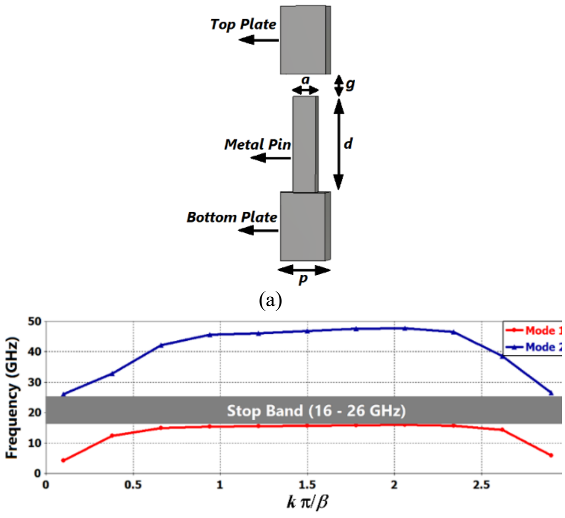

(b)

Fig.1. (a) Metal pin used in the groove gap-waveguide (GGW) filter, and (b) dispersion diagram of the GGW using the metal pin.

The metallic pins were strategically placed within the structure to form the cavity, as displayed on Fig.2. These pins serve a critical role in confining the EM modes within the cavity, ensuring efficient energy storage and transfer while minimizing unwanted mode interference. The placement and dimensions of the pins were key parameters in achieving the desired filter performance, as they directly influence the resonant frequencies and the formation of the EM bandgap.

TABLE I. DIMENSIONS OF THE GEOMETRICAL PARAMETERS OF THE METAL PIN.

| Parameters | Range | Exact value |
|---|---|---|
| Height of the pins (*d*) | $d \approx \lambda/4$ | $d = 4.25$ mm $\approx \lambda/4$ |
| Cross-sectional dimensions of the pins (*a*) | $\lambda/40 < a < \lambda/10$ | $a = 1$ mm $= \lambda/16$ |
| Period of the pins (*p*) | $\lambda/25 < p < \lambda/5$ | $p = 2$ mm $= \lambda/8$ |
| Gap between AMC & PEC (*g*) | $\lambda/20 < g < \lambda/10$ | $g = 1$ mm $= \lambda/16$ |

The groove/cavity region is realized by omitting pins to set the cavity width, depth and length to ensure it could support the desired wave propagation characteristics at the target frequency bands. In the 3rd order, the two cavity groups use $g_1 = 15$ mm and $g_2 = 29$ mm to target the two passbands at 19 and 20.75 GHz, while effectively attenuating frequencies outside this range. Coaxial excitation uses positions $L_p$= 6.5mm and $W_p$= 5.5 mm with penetration depth *pd*= 2 mm. In other words, besides the arrangement and dimensions of the metal pins for confining EM modes and achieving the desired bandgap characteristics, the placement of coaxial ports is another critical aspect of the design. Their separation from the lateral pins in both vertical and horizontal directions, as well as the depth to which the coaxial pins penetrate the cavity, have a significant impact on the resonator's performance, particularly on the S-parameter response. The S-parameter response is highly sensitive to these geometric parameters because they influence the coupling efficiency, insertion loss, and return loss of the resonator. A poorly optimized placement or depth can lead to undesirable resonances or signal attenuation, undermining the filter's performance. Therefore, precise optimization of these structural parameters is essential to ensure the resonator achieves high performance with minimal loss and strong selectivity at the target frequencies. The final optimized structural parameters, determined through extensive simulations and iterative adjustments, are summarized in Table II. These parameters ensure the resonator's ability to operate effectively within the specified frequency bands, meeting the design objectives for the GGW filter.

It is worth mentioning that, to enable signal coupling, coaxial ports were integrated into the design. These ports facilitate the efficient transfer of energy into and out of the filter, allowing the device to interface seamlessly with external circuits. The coupling mechanism was engineered by optimizing the inter-cavity spacing (*i*), the I-shaped slot dimensions ($C_1$–$C_4$), and the probe penetration depth using full-wave CST simulations to achieve the desired coupling strength while maintaining low insertion loss and high selectivity. This systematic and iterative design approach resulted in a filter structure with the required performance characteristics, demonstrating the efficacy of the groove gap-waveguide cavity and pin arrangement for dual-band operation in satellite communication systems.

The resonant unit of the proposed bandpass filter (BPF) is a dual-mode GGW resonant cavity, which exhibits resonant characteristics like those of a rectangular waveguide cavity. The resonant frequency of mode $mn$ can be calculated using the following expression [24]:

$$f_{mnp} = \frac{c}{2\pi}\sqrt{\left(\frac{m\pi}{l}\right)^2 + \left(\frac{n\pi}{w}\right)^2 + \left(\frac{n\pi}{h}\right)^2} \qquad (1)$$

where, *c* is the speed of light, *l*, *w*, and *h* are the length, width and height of the resonant cavity.

As indicated by Fig.2, the cavity resonator was excited via one of the coaxial ports located on the top plate, while the resonant signal was extracted through the other port. The cavity demonstrates passbands around 18.94 and 20.75 GHz, with an insertion loss of less than 1 dB and a return loss exceeding 15 dB. The electric field patterns of the resonant modes excited at 18.94 and 20.75 GHz within the GGW cavity are illustrated in Figs. 2(e) and 2(f), confirming the resonator's ability to support the intended dual-band operation by effectively guiding and confining EM energy at the desired frequencies.

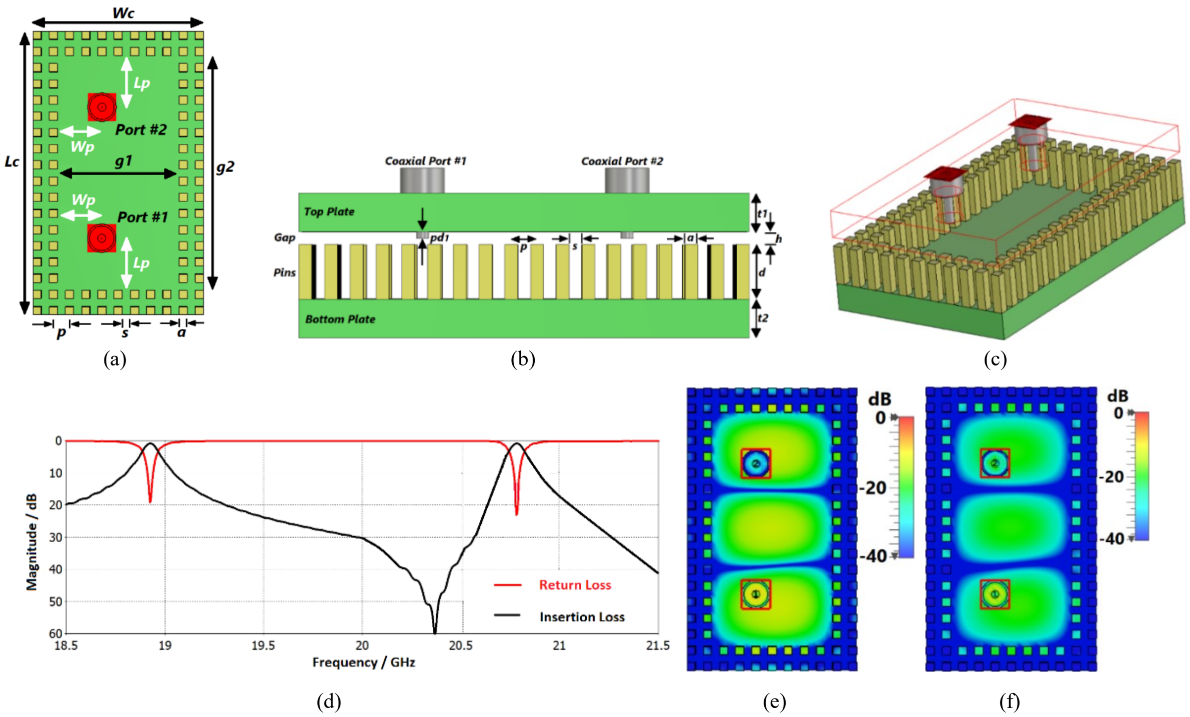


Fig.2. Configuration of the groove gap waveguide cavity resonator: (a) top view, (b) side view, (c) isometric view, (d) simulated return loss and insertion loss responses, and electric field distributions at resonance frequencies of (e) 18.93 GHz and (f) 20.75 GHz. The field distribution in (e) corresponds to a higher-order $TE_{103}$ mode, which was explored during the initial design phase for mode analysis but was not used in the final filter implementation.

TABLE II. OPTIMIZED STRUCTURAL PARAMETERS OF THE SINGLE CAVITY GROOVE GAP WAVEGUIDE

| Parameters | Value (mm) | Parameters | Value (mm) |
|---|---|---|---|
| *Lc* | 35.0 | $pd_1$ | 0.5 |
| *Wc* | 21.0 | $t_1$ | 3.0 |
| *Lp* | 6.5 | $t_2$ | 3.0 |
| *Wp* | 5.5 | *Lf* | 35.0 |
| $g_1$ | 15.0 | *Wf* | 63.0 |
| $g_2$ | 29.0 | *i* | 1.0 |
| *d* | 4.25 | *pd2* | 2.0 |
| *h* | 1.0 | *C1 (Fig.5)* | 19.0 |
| *p* | 2.0 | *C2 (Fig.5)* | 2.5 |
| *a* | 1.0 | *C3 (Fig.5)* | 1.0 |
| *s* | 1.0 | *C4 (Fig.5)* | 8.0 |

### *A) 3rd Order GGW Filter*

The synthesis of a filter with a specified passband requires cascading multiple resonators arranged in series to achieve the desired passband characteristics. The spacing between the resonators is critical, as it determines the coupling coefficients. The structure of the proposed third-order GGW filter is shown in Fig. 3. The design process began by establishing the physical dimensions of the cavity resonators to achieve resonances at 19 and 20.75 GHz. During this process, it was observed that coupling between adjacent resonators could shift the resonance frequencies of the cavities. To evaluate and quantify this frequency shift, an eigenmode analysis was performed using CST Microwave Studio. The optimized dimensions of the resonators were determined as $g_1$ = 15.0 mm and $g_2$ = 29.0 mm. To synthesize the desired frequency response, the coupling matrix approach outlined in [23] was used. This approach is independent of the physical structure and relates the coupling coefficient ($M_{ij}$) between cavities to the fractional bandwidth (FBW), as described in [25]:

$$M_{ij} = \left(\frac{f_1^2 - f_2^2}{f_1^2 + f_2^2}\right) \times \frac{1}{FBW} \qquad (2)$$

where $f_1$ and $f_2$ are the resonant frequency obtained from eigenmode analysis of the structure using CST Microwave studio.

For a fractional bandwidth of 1.25% in the first passband, the coupling coefficients between two adjacent resonators, $M_{12}$ and $M_{23}$, are calculated to be 1.10. Based on the graph in Fig. 4, obtained from simulation analysis using CST Microwave Studio, the gap between the cavities required to achieve the desired coupling is determined to be 3 mm. The physical interval ($i$) between adjacent resonators was then optimized to realize the desired passband response. This optimization was conducted using CST Microwave Studio's tools, with a cost function defined to minimize return loss within the passband while maximizing rejection outside it. The cost function is determined as follows. Let $B_1$ = [18.90, 19.13] GHz and $B_2$ = [20.55, 20.83] GHz denote the target passbands (Fig. 3(e)), and let $S_L$, $S_M$, and $S_H$ denote the stopbands below $B_1$, between $B_1$, $B_2$, and above $B_2$, respectively. For a given parameter set (here the spacing $i$), we compute the simulated S-parameters and minimize

$$J(i) = w_{RL}\sum_{k=1}^{2}\frac{1}{|B_k|}\sum_{f\in B_k}[max\{0,|S_{11}(f)|-\tau_{RL}\}]^2 + w_{IL}\sum_{k=1}^{2}\frac{1}{|B_k|}\sum_{f\in B_k}[max\{0,\tau_{IL}-|S_{11}(f)|\}]^2 + w_{SB}\frac{1}{|S_L\cup S_M\cup S_H|}\sum_{f\in S_L\cup S_M\cup S_H}[max\{0,|S_{21}(f)| - \tau_{SB}\}]^2 + w_{CF}\sum_{k=1}^{2}\left(\frac{f_{pk,k}(i)-f_{0,k}}{FBW_k f_{0,k}}\right) \quad (3)$$

where $f_{0,1}$ = 19.0 GHz, $f_{0,2}$ = 20.75 GHz are the target centers (Fig. 3(e)), $f_{pk,k}(i)$ is the simulated passband peak, and $FBW_k$ is the target fractional bandwidth of each passband (from the coupling-matrix synthesis and Fig. 4). The thresholds are set in linear magnitude as τRL = $10^{-15/20}$ (return-loss target 15 dB), $\tau_{IL} = 10^{-0.8/20}$ (in-band insertion-loss target 0.8 dB), and $\tau_{SB} = 10^{-30/20}$ (stopband attenuation target 30 dB). Weights $w_{RL}$, $w_{IL}$, $w_{SB}$, $w_{CF}$ are chosen so that out-of-band suppression and in-band matching have comparable influence, with a slightly higher weight on $w_{SB}$ to enforce inter-band isolation. The grids $B_1$, $B_2$, $S_L$, $S_M$, $S_H$ are uniformly sampled within the EBG window and measured span shown in Fig.3 and used consistently with the coupling-versus-distance characterization in Fig.4. The electric field distribution of the modes excited in the cavities of the filter structure is shown in Fig. 3(d). It is evident the excitation is strongest in the input and output cavities, indicating the weak coupling between the cavities. The optimum observed for this design is $i$ = 1 mm, which achieves the dual-band response in Fig.3(e). This figure shows the response of the baseline third-order GGW filter configuration prior to the introduction of the I-shaped coupling channels discussed in Section II-B. The 3-dB passband covers 18.9–19.15 GHz and 20.82–20.87 GHz with center frequencies of 19.11 and 20.8 GHz, corresponding to fractional bandwidths of 1.31% and 0.24%, respectively. The filter has an insertion loss better than 1.85 dB, with approximately 0.4 dB at the center frequencies of 19.11 and 20.8 GHz. The measured return loss across the passbands exceeds 15 dB, indicating good impedance matching suitable for practical applications. There is a 4.8% discrepancy between the theoretical and measured fractional bandwidth.

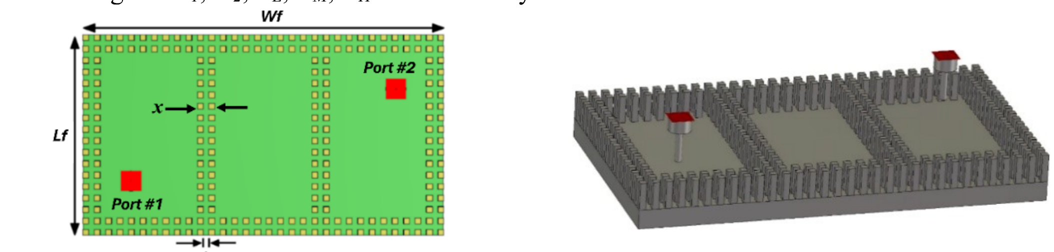


(a)

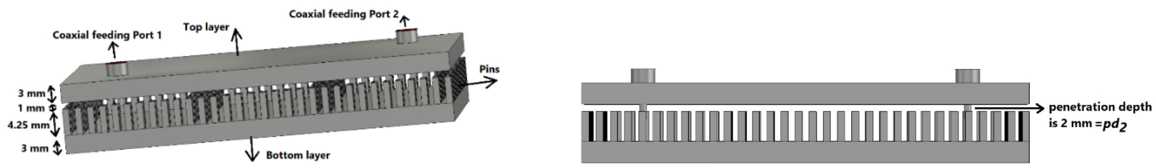


(b)

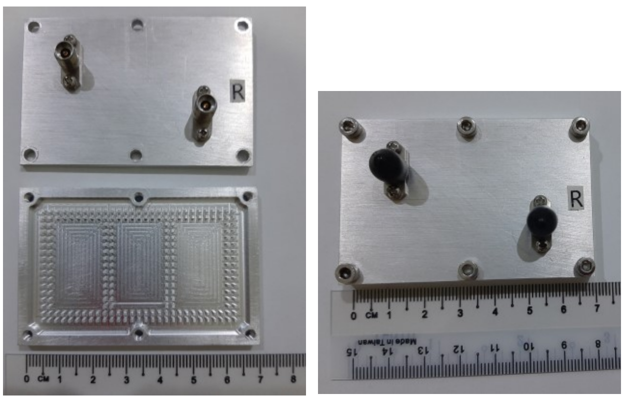

(c)

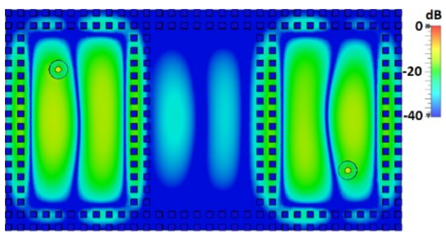


(d)

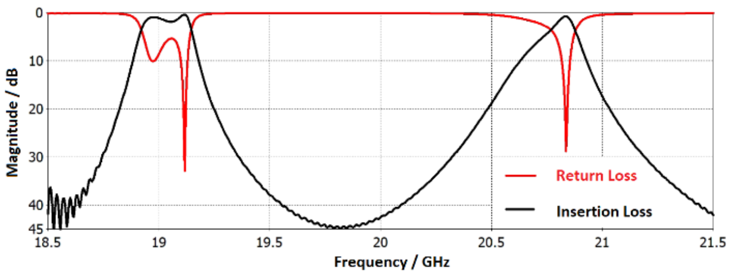


(e)

Fig.3. Baseline third-order groove gap waveguide filter prototype with a flat (non-engraved) lid, prior to the introduction of the I-shaped coupling channels used in the final design of Fig.5: (a) top view (left) and isometric view (right) with the top layer hidden, showing the inter-resonator spacing '*i*'; (b) side views from different angles to illustrate all structural parameters (left) and the penetration depth of the coaxial probe (right); (c) fabricated prototype before assembly (left) and after assembly (right); (d) simulated electric field distribution at 19 GHz within the filter structure, showing the selected $TE_{102}$ resonance mode; and (e) measured return loss and insertion loss responses. The $TE_{102}$ mode provides enhanced field symmetry and coupling characteristics, enabling stable dual-passband operation in the final filter design. The periodic pin structures in (a) represent the EM bandgap walls typical of GGW technology, used to confine the wave and eliminate the need for metallic sidewalls.

### *B) Performance Enhancement Via Inter Cavity Coupling*

Before introducing the enhanced coupling structure, it is important to note that Fig. 3 presents the baseline third-order GGW filter prototype without the I-shaped coupling channels. In this configuration, the top metallic plate is a flat lid without engraved cavities and was used to evaluate the initial dual-band cavity behavior. Fig. 5, in contrast, presents the final optimized prototype where I-shaped channels are engraved on the underside of the lid to introduce additional inter-cavity coupling and improve the filter's impedance matching and insertion loss.

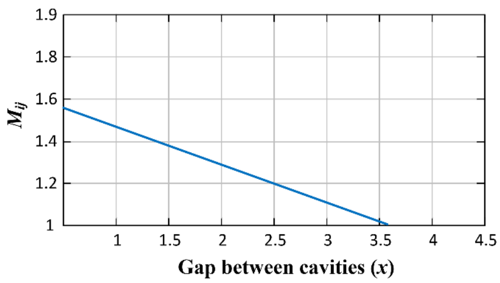


Fig.4. Coupling coefficient between two adjacent cavities versus distance ($x$).

A key contribution of this work is the introduction of I-shaped coupling slots engraved on the underside of the top plate to control inter-cavity coupling in the proposed GGW filter. Two I-shaped channels were milled on the underside of the top plate in strategic locations, as illustrated in Fig. 5, to create electromagnetic coupling between the outer cavities and partial coupling with the middle cavity. The purpose of the proposed coupling channels is to introduce additional boundary conditions and modify the EM field distribution leading to new field distributions that better suit the desired filter response.

Contrary to the interpretation that the dual-band response arises from sequential modes of a single cavity, the proposed filter employs two distinct cavity groups, each operating in the same $TE_{102}$ mode but with different physical dimensions ($g_1$ and $g_2$) to support independent resonances at 19 and 20.75 GHz. This allows separate control of the center frequency and bandwidth of each passband. The use of identical mode types avoids the limitations associated with relying on higher-order or sequential modes, which are inherently frequency-locked and do not permit independent tunability.

This mode provides a favorable field distribution that facilitates efficient coupling via the I-shaped slots, with reduced sensitivity to fabrication tolerances. The I-shaped coupling slots were aligned and dimensioned to preferentially couple $TE_{102}$ while discouraging coupling to undesired modes. Although the fundamental $TE_{101}$ mode offers a more compact footprint, it was not chosen due to limitations in coupling efficiency, reduced field symmetry, and proximity to spurious modes that could compromise filter selectivity. In contrast, the $TE_{102}$ mode provides two longitudinal electric-field maxima along the cavity length, enabling stronger and more controllable coupling through the I-shaped slots while improving isolation between adjacent resonators. The $TE_{102}$ mode allows greater spatial separation of field maxima, improving isolation between adjacent cavities and enabling dual-passband operation with minimal mutual interference. This choice is also supported by simulation results, as illustrated in Fig.3, which confirm clean resonance and strong confinement at the target frequencies. The chosen configuration enables a practical dual-band filter with flexible frequency planning for satellite communication links. The dimensions and characteristics of these I-shaped channels were optimized through 3D EM simulations conducted using CST Microwave Studio. The GGW filter, shown in Fig.5, was fabricated using a subtractive manufacturing method with a CNC machine. The resulting design not only improves spectral performance but also simplifies fabrication, as the slots can be milled into a single metal plate without requiring multilayer alignment or complex machining.

The S-parameter response of the 3rd order GGW filter with I-shaped coupling, depicted in Fig.5, demonstrates significant performance improvements.

The 3-dB passbands now extend from 18.90–19.13 GHz and from 20.55–20.83 GHz with an insertion loss of less than 0.4 dB. The S-parameters were measured using a calibrated vector network analyzer with the reference planes located at the ends of the measurement cables; therefore, cable and connector losses are calibrated out, while the reported insertion loss includes the coaxial probe transitions integrated with the filter prototype. Additionally, the return loss exceeds 15 dB indicating effective signal management. A comparison of simulated and measured results confirms the high accuracy and reliability of the proposed method. The small shifts observed between simulated and measured center frequencies are consistent with the machining tolerance of the CNC process (≈±50–100 μm), which aligns with the trends predicted in the sensitivity analysis. Simulated and measured S-parameters show only the two target passbands within the 16–26 GHz EBG window, and tolerance studies indicate that realistic dimensional deviations detune and affect matching but do not create new passbands, supporting the absence of spurious-mode excitation in the reported operating bands. The physical prototype, assembled filter, and experimental setup are also shown in Fig.5.

The 3-dB bandwidth of each passband is controlled by tuning the inter-resonator coupling coefficient through adjustment of the cavity spacing ($i$) and the dimensions of the I-shaped coupling slots, as determined by coupling-matrix synthesis and full-wave EM optimization. Specifically, the fractional bandwidth is directly related to the coupling coefficients, which are realized by adjusting the physical gap between cavities and by introducing I-shaped coupling channels on the top metallic plate. These slots perturb the cavity modes and create the required EM interaction. Additionally, the placement and penetration depth of the coaxial probes affect the loaded quality factor (Q), which further influences the bandwidth. Therefore, by tuning these structural parameters during the design phase, the bandwidth of each passband can be independently and accurately controlled.

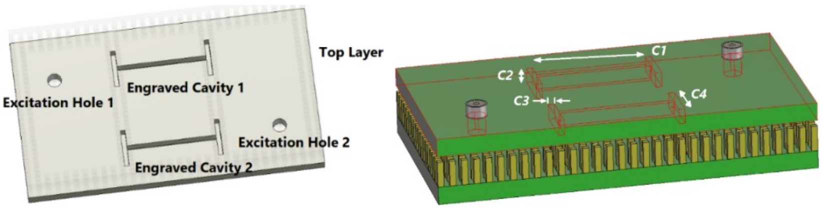


(a)

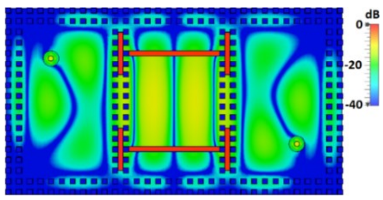


(b)

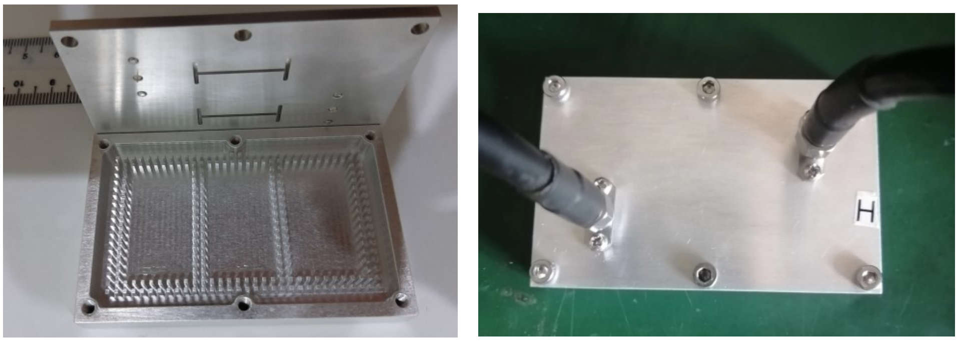

(c)

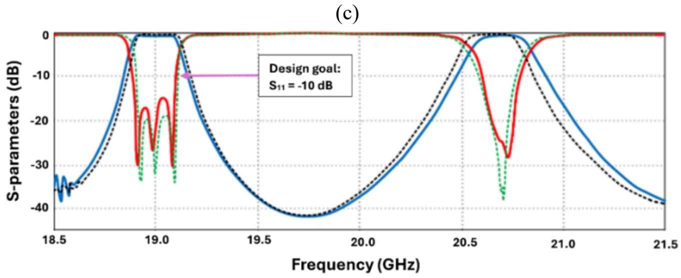


(d)

Fig.5 Final optimized GGW filter incorporating the proposed I-shaped coupling slots (key coupling mechanism of this work). (a) schematic layout of the balanced third-order groove gap waveguide filter highlighting the I-shaped hollows etched on the top layer and their dimensional parameters, where all other parameter values are the same as in Fig. 2; (b) E-field distribution at 19 GHz in the filter structure with the top plate including I-shaped channels; (c) manufactured prototype before assembly (left) and after assembly (right); and (d) simulated (dashed lines) and measured (solid lines) return-loss and insertion-loss responses. Dimensions of the structural parameters *C1*–*C4* are listed in Table II.

The design flowchart of the proposed dual-band GGW filter is given in Fig.6. Once fabricated, the bandwidths are fixed, making the design highly sensitive to dimensional tolerances.

To assess the robustness of the proposed filter design, a parameter sensitivity analysis was conducted using CST Microwave Studio. The following key geometrical parameters were varied around their optimized values to evaluate their influence on the filter's performance, particularly the center frequency, 3-dB bandwidth, insertion loss, and return loss:

- *Pin Height* (*d*): Varying the pin height by ±0.1 mm around the nominal 4.25 mm value resulted in a shift of the bandgap and a ±70 MHz change in center frequency. Lower pin heights decreased mode confinement, slightly increasing insertion loss.
- *Air Gap* (*g*): A ±0.1 mm variation in the air gap above the pins (nominal *g*=1 mm) led to detuning of the passband and degradation in return loss. Larger gaps weakened the effective PMC boundary condition, increasing EM leakage.
- *Cavity Dimensions* ($g_1$, $g_2$): The cavity width ($g_1$) and length ($g_2$) were each varied by ±0.2 mm. This resulted in shifts of approximately ±50–80 MHz in center frequency, confirming their critical role in frequency tuning.
- *Coupling Gap* (*i*): The spacing between resonators, '*i*', directly controls coupling strength. A variation of ±0.2 mm caused ~0.1–0.2% change in 3-dB bandwidth, consistent with coupling coefficient trends in Fig.4.
- *I-Shaped Slot Parameters* ($C_1$-$C_4$): Each slot dimension was varied by ±0.1 mm. These perturbations had significant effects on return loss and selectivity. Return loss degraded by over 5 dB for some configurations, confirming the importance of precise milling.

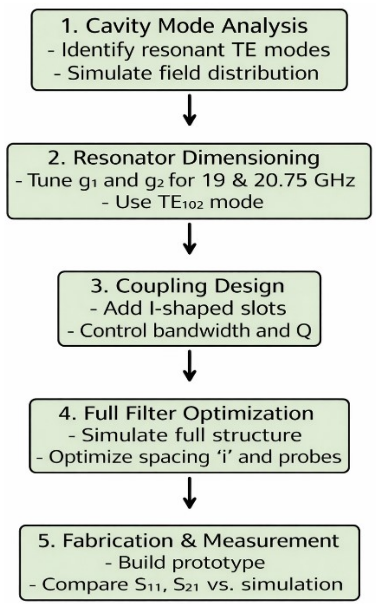


Fig.6. Design flowchart of the proposed dual-band groove gap waveguide filter. The process includes mode identification, dimension tuning for dual $TE_{102}$-mode cavities, coupling structure design, full-wave optimization, and experimental validation.

Fig.7 illustrates the influence of pin height on the center frequencies of the two passbands. Fig. 8 shows how the return loss and 3-dB bandwidth vary with the inter-cavity gap, while Fig. 9 presents the relationship between the air gap and insertion loss. Finally, Fig. 10 demonstrates the sensitivity of return loss to variations in the width of the I-shaped coupling slot ($C_1$). These results confirm that precise fabrication is essential to ensure performance consistency. They also highlight that while the proposed filter is moderately tolerant to small geometric variations, manufacturing precision is essential to maintain performance especially given the non-tunable nature of groove gap waveguide structures.

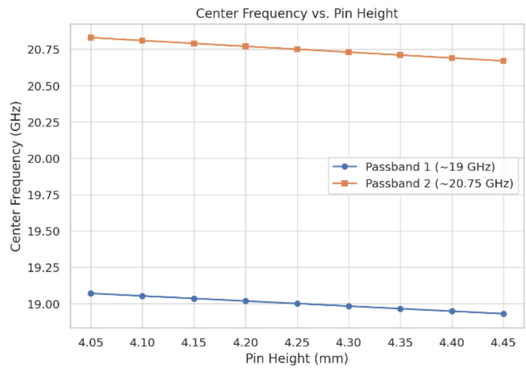


Fig.7. Variation in center frequency with changes in pin height *d*. Both passbands shift approximately ±70–80 MHz for ±0.2 mm change, indicating strong dependence on pin dimensions.

In the proposed filter, I-shaped slots are employed as the primary coupling mechanism between adjacent resonators. This decision is driven by their ability to locally perturb the EM field distribution, enabling efficient energy exchange between cavities while maintaining a compact footprint. Compared to conventional rectangular or circular apertures, I-shaped slots offer greater control over both the coupling strength and the frequency selectivity due to their extended surface area and asymmetrical geometry. This geometry facilitates stronger electric field concentration at slot edges, which enhances inter-cavity coupling without significantly altering the individual resonant frequencies.

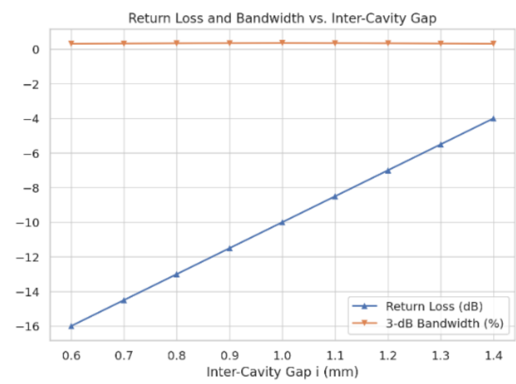


Fig.8. Return loss and 3-dB bandwidth as functions of inter-cavity spacing *i*. Optimal performance occurs around *i* =1.0 mm; deviations reduce selectivity and impedance matching.

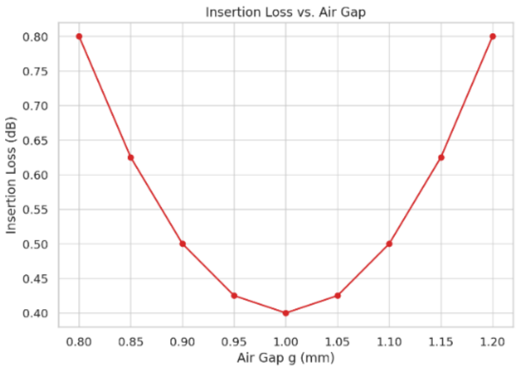


Fig.9. Insertion loss versus air gap $g$ between the top and bottom plates. Insertion loss increases significantly as the air gap deviates from the 1 mm design target.


Fig.10. Return loss sensitivity to variation in I-shaped slot width $C1$. Deviations of ±0.1 mm degrade return loss by more than 5 dB, underscoring the importance of precise slot machining.

### *C) Fabrication Considerations and Sensitivity Analysis*

The proposed filter was fabricated using precision CNC milling of two aluminum blocks, forming the base and top metallic plates. The air gap between the pin tops and the top metal plate was maintained at approximately 1 mm ($\lambda/16$), which is critical for achieving the intended bandgap and suppressing parallel-plate modes. During assembly, alignment dowel pins and uniformly tightened screws were used to maintain plate parallelism, ensuring a nearly constant air gap $g \approx 1$ mm across the structure. The bottom plate includes the array of rectangular pins that define the EM bandgap structure, while the top plate includes the I-shaped coupling slots and provides the air gap needed for mode confinement. The material choice of aluminum offers a balance between conductivity, weight, and mechanical machinability, making it suitable for space-grade components.

Special attention was given to maintaining uniform pin height (nominally 4.25 mm) and precise slot dimensions to ensure consistent resonance behavior. Mechanical fixtures were used to align the plates during assembly to avoid lateral or vertical misalignment that could affect performance.

To validate the design's robustness to fabrication tolerances, a detailed sensitivity analysis was performed (see Figs. 7–10). The results demonstrate that the filter retains acceptable performance despite moderate dimensional variations, confirming its resilience to typical machining inaccuracies.

### *D) Proof of Leakage and Surface-Wave Suppression*

*Modal bandgap evidence.* The dispersion analysis of the pin unit-cell in Fig.1 shows a stopband from 16–26 GHz for the adopted lattice $d$ = 4.25 mm, $a = g = 1$ mm, $p$ = 2 mm. Within this band, parallel-plate and surface waves are evanescent, which prevents lateral leakage when the lid spacing is $g<\lambda/4$. This is the established operating principle of gap-waveguides with a PEC–PMC pair formed by the bed-of-nails lattice.

*Field-confinement evidence*. Full-wave simulations show energy confined to the groove/cavities with negligible fields in the pin bed. The E-field map in Fig.3 at 19 GHz illustrates this confinement for the operating $TE_{102}$ cavity mode. The measured response in Fig.5 exhibits insertion loss < 0.4 dB across both passbands, which is consistent with minimal radiation loss and suppressed surface-wave power.

*Parametric consistency*. The sensitivity study shows that relaxing the effective PMC condition degrades confinement: increasing the air gap $g$ detunes the passband and raises insertion loss (Fig.9), and reducing pin height $d$ weakens the bandgap and shifts the centers (Fig.7). Both trends are expected when leakage and surface-wave suppression deteriorate, providing indirect empirical support for the mechanism.

Taken together, the unit-cell stopband, the confined field patterns with low measured loss, and the tolerance trends constitute direct and self-consistent proof that the GGW lattice suppresses radiation leakage and surface-wave propagation in the reported bands.

During assembly, the two aluminum halves were aligned with mechanical fixtures to prevent lateral and vertical misregistration, and the lid spacing was maintained at approximately $g$=1 mm. Photos of the prototype before and after assembly are shown in Fig.5. Sensitivity results indicate that deviations affecting $g$ (from tilt or $z$-offset) degrade matching and increase insertion loss, while lateral slip that perturbs the inter-cavity spacing $i$ or the I-slot registration alters bandwidth and return loss. Specifically, $g \pm 0.1$ mm detunes the passbands and worsens return loss; $i \pm 0.2$ mm changes the 3-dB bandwidth by about 0.1–0.2%; and $C_1 \pm 0.1$ mm can reduce return loss by more than 5 dB. The measured S-parameters in Fig.5 remain close to simulation with approximately 0.4 dB insertion loss, indicating that assembly alignment was kept within these tolerance bounds.

### *E) Manufacturing and Cost Considerations for K-band Mass Production*

*Implications for process capability*. To keep re-tune scrap low at K-band, practical targets are: flatness/parallelism of the mating plates ≤ 20–30 µm over the cavity region to stabilize $g \approx 1$ mm, critical features (pin height $d$, slot width $C_I$, probe penetration) held within ±50–100 μm (tighter on $g$, $C_I$), and surface roughness Ra ≤ 1.6 μm on RF faces. These values align with the observed sensitivity of $g$, $d$, $C_I$ to loss and match.

*Manufacturing routes and trade-offs*. Multiple routes can meet these tolerances; selection depends on volume and allowed tooling. A broad fabrication overview for GWG/GGW components is given in the literature.

• *CNC milling (baseline*). Two aluminum halves with dowel-pin registration and post-op surfacing; this is the route used for our prototype [33].

• *Investment casting + finish-machining*. Near-net pin beds and cavities from lost-wax casting, then finish-mill pins, slots, and sealing lands to tolerance for mid/high volumes [34].

Yield is dominated by the air gap $g$ and the I-slot geometry. We recommend hardened dowel pins and pilot shoulders for *x–y*, shim stock or precision spacers under fasteners to set $g$ within ±50 μm, torque sequencing to preserve flatness, and CMM or optical profilometry to verify pin height and slot widths on a sampling basis. These controls directly target the most sensitive parameters identified above.

Tight control of $g$ and $C_I$ is essential; employ go/no-go slot gauges and calibrated spacers for $g$. Thermo-mechanical stability of aluminum implies $\Delta g$ with temperature, evaluate hard coat anodize or alternative alloys, and plan thermal cycling as part of environmental screening. Connectorization can be a yield limiter; consider waveguide or SMPM launches to reduce variance relative to hand-set coax probes.

Absolute costs are location and supplier dependent, so we quote relative indices and main drivers, consistent with mm-wave packaging practice.

### *F) Power handling considerations (air-filled GGW vs. dielectric-filled)*

For continuous-wave (CW) operation, two limits dominate: (i) RF breakdown/multipaction (a field limit) and (ii) ohmic/dielectric heating (a thermal limit). With respect to field limit, in air at 1 bar, the RF breakdown strength is commonly taken near 3 MV/m (≈ 30 kV/cm). Using the standard $TE_{10}$ waveguide power relation that links maximum electric field to carried power, the theoretical air-breakdown limit in a K-band rectangular guide is far above typical IoT transmit powers; practical limits are reduced by field enhancement at edges/slots and by discontinuities. For space use (vacuum), multipaction becomes the governing mechanism; design and qualification should follow ECSS-E-HB-20-01A (analysis + test) [35], which gives the process for establishing a multipaction-free operating margin for the exact geometry and carrier(s).

With respect to thermal limit of the proposed prototype, our measured insertion loss is < 0.4 dB in both bands (Fig.5). Thus, the dissipated power is $P_{\text{diss}} = P_{\text{in}}(1-10^{-0.4/10}) \approx 0.089P_{\text{in}}$. As a result, 10 W CW at the input corresponds to ≈ 0.9 W total dissipation spread over the cavities and slots; with the present aluminum body and footprint, this is comfortably within conduction cooling capacity. 20 W CW would dissipate ≈ 1.8 W and remain feasible with modest heatsinking; above this, thermal gradients may detune the narrowband and should be verified by thermal-mechanical analysis.

Compared with dielectric-filled filters, an air-filled GGW does not incur bulk dielectric loss, so it avoids the temperature rise associated with the material's loss tangent. At K-band, that dielectric loss often becomes the dominant limit under continuous-wave operation, meaning dielectric-loaded filters of comparable size generally reach thermal derating at lower input power. This is true even though many ceramics have high intrinsic electric-field breakdown strengths, the bottleneck is typically heat generated by dielectric loss, not the breakdown field itself.

## III. State-of-the-Art Comparison

This section positions the proposed single-layer dual-band GGW filter against representative GGW/RGW variants across Ku–K–mm-wave bands. We compare footprint (normalized to $\lambda_0^2$), 3-dB fractional bandwidth (FBW), in-band insertion loss (IL), return loss (RL), and implementation complexity.

Compared with [26], which uses a T-shaped region densely filled with pins, our design is markedly simpler to machine and smaller in normalized area. The filter in [26] exhibits a large footprint (14.9×4.08 $\lambda_0^2$), higher IL (1.0 dB), narrow FBW (0.62%), and RL of 10 dB. The mushroom-pin and microstrip-ridge realizations [27]–[29] gain compactness in places but at the cost of higher IL (1.29–1.37 dB) and added fabrication steps (via holes, multilayer substrates, precision mushroom features). The three-layer rectangular-pin/X-iris GGW in [30] achieves excellent IL (0.24 dB) but only 2.38% FBW and higher structural complexity. Pin-free regions with hollowed inductive coupling in [1] keep IL around 1.1 dB with narrow FBW (1.4%) and a larger footprint, while the single-channel inductively coupled GGW in [31] shows moderate bandwidth (4.19%) and IL (1.5%) but still demands precise pin placement.

Two recent dual-band references strengthen the comparison. At Ku-band, [36] reports reflectionless single/dual-band GGW filters (14.52/15.2 GHz) with measured IL of 0.79/0.76 dB and FBW of 2.26/1.95%, obtained using stacked structures and absorptive networks, solid RF figures but high complexity. At mm-wave, [37] demonstrates a multilayer GGW dual-mode dual-band filter (~67.9/69.8 GHz) that is extremely compact (0.83×0.45 $\lambda_0^2$) but with narrower FBW (0.63/0.57%) and higher IL (1.98/2.12 dB), reflecting tighter tolerances and losses at ~70 GHz.

Within this context, our K-band prototype achieves a balanced trade-off: compact single-layer construction (4.20×2.33 and 4.50×2.50 $\lambda_0^2$), low IL (0.37/0.39 dB), RL ≈ 16 dB, and FBW ≈ 1.3%. Avoiding multilayer alignment, dense mushroom fields, and absorptive networks reduces fabrication risk and cost while retaining per-band tunability. To pursue wider FBW with this topology, stronger inter-cavity coupling (reduced spacing or modified slot geometry) and possibly smaller pin cross-sections would be required, both driving tighter machining tolerances than our present facility supports.

The reported prototype was characterized at room temperature under laboratory conditions. The tolerance study in Section II indicates that modest dimensional deviations in pin height, air gap, inter cavity spacing, and slot geometry affect the passbands in predictable ways, which guided our machining tolerances. However, comprehensive environmental assessments such as thermal cycling, thermal vacuum, vibration and shock, and long-term stability were not part of this work and remain to be evaluated for satellite deployments.

## IV. Practical Applications

The proposed dual-band GGW filter can serve as a building block for frequency-partitioned K-band satellite IoT payloads. The two passbands centered at 19.0 GHz and 20.75 GHz could conceptually support different traffic classes or link requirements within a satellite communication system. For example, one band may be allocated to coverage-oriented IoT services with moderate data rates, while the other could support higher-density or higher-throughput links. The low insertion loss, compact single-layer structure, and suppression of parasitic leakage provided by the GGW implementation make the filter suitable for integration into K-band front-end architectures where efficient spectral separation is required. The exact allocation of frequency bands and services ultimately depends on system-level considerations such as link budgets, regulatory constraints, and network architecture.

## V. Conclusion

This paper presented a dual-passband groove gap waveguide (GGW) filter for K-band satellite communication links, emphasizing compactness, low insertion loss, and simplified manufacturability. The proposed design employs two cavity groups operating in the $TE_{102}$ mode within a single-layer GGW structure. Inter-resonator coupling is implemented through I-shaped slots engraved on the top plate, which act as the primary mechanism for controlling coupling and enabling independent tuning of the two passbands. The cavity structure is formed using a periodic metallic pin lattice that suppresses parallel-plate modes and ensures strong electromagnetic confinement, while coaxial probes provide practical excitation.

Measured results at room temperature confirm dual-band operation centered at 19.0 and 20.75 GHz with 3-dB bandwidths of approximately 400 MHz and 280 MHz, respectively. The prototype achieves insertion loss below 0.4 dB in both passbands and return loss better than 15 dB, demonstrating excellent agreement between simulated and measured responses. The single-layer implementation reduces assembly complexity compared with multilayer or stacked GGW filters, requiring only two metallic parts while maintaining high-Q cavity performance and robust electromagnetic confinement.

Sensitivity analysis further indicates that the proposed structure maintains acceptable performance under typical machining tolerances, supporting practical implementation using standard CNC fabrication processes. These results demonstrate that the proposed dual-band GGW filter can serve as a compact and low-loss building block for multiband K-band RF front ends in satellite IoT communication systems.

Future work will focus on evaluating environmental robustness and long-term reliability through thermal cycling, vibration testing, and extended operation, as well as exploring stronger inter-resonator coupling schemes to achieve wider fractional bandwidth and enhanced selectivity. Additional studies will also investigate alternative transitions and integration with multiplexing networks to further extend the applicability of the proposed architecture in advanced satellite payloads.

TABLE III. PERFORMANCE COMPARISON OF THE PROPOSED FILTER WITH PRIOR ARTS.

| Reference | Dimensions ($\lambda_0^2$) | Technology | $f_0$ (GHz) | 3-dB FBW (%) | Return loss (dB) | Insertion loss (dB) | Metal layers | Number of assembly parts | Complexity |
|---|---|---|---|---|---|---|---|---|---|
| [1] | 2.55 × 5.43 | GGW | 65.0 | 1.40 | 12.5 | 1.10 | 2 | 2 | Low |
| [26] | 14.9 × 4.08 | RGW | 11.6 | 0.62 | 10.0 | 1.00 | 2 | 2 | Low |
| [27] | 3.29 × 2.26 | MS-RGW | 14.8 | 5.50 | 10.0 | 1.35 | 3 | 2 | Moderate |
| [28] | 2.93 × 1.93 | MS-RGW | 21.0 | 4.72 | 14.18 | 1.37 | 3 | 2 | Moderate |
| [29] | 0.52 × 0.29 | PRGW | 12.0 | 8.30 | 25.0 | 1.29 | 3 | 2 | Moderate |
| [30] | 2.18 × 2.18 | GGW | 25.2 | 2.38 | 15.0 | 0.24 | 3 | 3 | Moderate |
| [31] | 4.62 × 0.80 | GGW | 17.33 | 4.19 | 15.0 | 1.50 | 2 | 2 | Low |
| [36] | 7.59 × 4.40 | GGW | 14.52 / 15.2 | 2.26 / 1.95 | 17 / 10 | 0.79 / 0.76 | 4 | 3 | High |
| [37] | 0.83 × 0.45 | GGW | 67.9 / 69.8 | 0.63 / 0.57 | 9.5 / 21.0 | 1.98 / 2.12 | 4 | 3 | High |
| **This work** | **4.20 × 2.33** | **GGW** | **19.0** | **1.32** | **16.0** | **0.37** | **2** | **2** | **Low** |
| **This work** | **4.50 × 2.50** | **GGW** | **20.75** | **1.26** | **16.0** | **0.39** | **2** | **2** | **Low** |

## REFERENCES


[1] M. Rezaee and A. U. Zaman, "Groove gap waveguide filter based on horizontally polarized resonators for V-band applications," *IEEE Trans. Microw. Theory Techn.*, vol. 68, no. 7, pp. 2601–2609, Jul. 2020.

[2] R. V. Snyder et al.,"Emerging trends in techniques and technology as applied to filter design," *IEEE J. Microwaves*, vol. 1, no. 1, pp. 317–344, Jan. 2021.

[3] Y. Sung, "Circular slot antenna with pattern diversity," *J. Electromagn. Eng. Sci.*, vol. 25, no. 1, pp. 54–61, 2025.

[4] C.-F. Chen et al., "Flexible design method for multifunctional filtering diplexers integrated with single-pole double-throw switches," *IEEE Access*, vol. 12, pp. 13502–13512, 2024.

[5] L. Nouri et al., "Novel energy harvesting microstrip lowpass-bandpass diplexer with an ultra-compact size for GSM and 5G communication systems," *AEU - Int. J. Electron. Commun.*, vol. 179, p. 155342, 2024.

[6] M. Rabbanifard et al.,"Design of compact and wideband groove gap waveguide-based directional couplers," *IEEE Access*, vol. 12, pp. 86346–86354, 2024.

[7] J. Liu et al.,"A hybrid architecture 360° phase shifter with continuously tunable phase shift and low in-band phase error," *IEEE Trans. Microw. Theory Techn.*, vol. 72, no. 8, pp. 4810–4821, Aug. 2024.

[8] E. Kim, Y. Kim, and S. Jeon, "A CMOS vector-sum phase shifter for 5G mm-wave application," *J. Electromagn. Eng. Sci.*, vol. 22, no. 1, pp. 8–11, 2022.

[9] M. Alibakhshikenari et al., "Innovative UWB phase shifters using groove gap-waveguide technology inspired by metasurfaces for beamforming networks operating at 100 GHz," in *Proc. 36th IEEE Asia-Pacific Microw. Conf. (APMC)*, Bali, Indonesia, Nov. 2024, pp. 740–742.

[10] M. Z. Iskandarani, "Investigation of energy consumption in WSNs within enclosed spaces using beamforming and LMS (BF-LMS)," *IEEE Access*, vol. 12, pp. 63932–63941, 2024.

[11] N. Qasem, "Exploring 60 GHz millimeter-wave indoor propagation path loss models and capacity enhancement for modified indoor environments," *J. Commun.*, vol. 19, no. 7, pp. 340–349, 2024.

[12] N. Qasem and M. Alkhawatrah, "60 GHz millimeter-wave indoor propagation path loss models for modified indoor environments," *Int. J. Electr. Comput. Eng.*, vol. 14, no. 3, pp. 2737–2752, 2024.

[13] D. Panusch, L. Pelchen, S. Müller, and G. Gold, "A novel manufacturing method for microwave components by lost wax casting," *IEEE Access*, vol. 11, pp. 25298–25302, 2023.

[14] K. K. Samanta and K. Aygün, "Microwave/millimeter-wave packaging for 5G and beyond: Materials, technologies, and techniques [From the Guest Editors' Desk]," *IEEE Microw. Mag.*, vol. 23, no. 8, pp. 46–49, Aug. 2022.

[15] P.-S. Kildal, "Waveguides and transmission lines in gaps between parallel conducting surfaces," EP Patent 20 080 159 791, Jul. 7, 2009.

[16] A. Berenguer et al., "Propagation characteristics of groove gap waveguide below and above cutoff," *IEEE Trans. Microw. Theory Techn.*, vol. 64, no. 1, pp. 27–36, Jan. 2016.

[17] P.-S. Kildal et al., "Design and experimental verification of ridge gap waveguide in bed of nails for parallel-plate mode suppression," *IET Microw. Antennas Propag.*, vol. 5, no. 3, pp. 262–270, Feb. 2011.

[18] H. Raza et al.,"Microstrip-ridge gap waveguide – study of losses, bends, and transition to WR-15," *IEEE Trans. Microw. Theory Techn.*, vol. 62, no. 9, pp. 1943–1952, Sep. 2014.

[19] Y. Shi et al., "Gap waveguide technology: An overview of millimeter-wave circuits based on gap waveguide technology using different fabrication technologies," *IEEE Microw. Mag.*, vol. 24, no. 1, pp. 62–73, Jan. 2023.

[20] W. Tan et al., "Low-cost gap waveguide technology using shallow grooves and glide-symmetric semicircular-holes EBG structures," *IEEE Antennas Wireless Propag. Lett.*, vol. 22, no. 12, pp. 2901–2905, Dec. 2023.

[21] A. Tamayo-Domínguez et al., "Groove gap waveguide in 3-D printed technology for low loss, weight, and cost distribution networks," *IEEE Trans. Microw. Theory Techn.*, vol. 65, no. 11, pp. 4138–4147, Nov. 2017.

[22] M. M. M. Ali, et al., "Graphene-based terahertz reconfigurable printed ridge gap waveguide structure," *Sci. Rep.*, vol. 12, 2022.

[23] A. U. Zaman, P.-S. Kildal, and A. A. Kishk, "Narrow-band microwave filter using high-Q groove gap waveguide resonators with manufacturing flexibility and no sidewalls," *IEEE Trans. Compon. Packag. Manuf. Technol.*, vol. 2, no. 11, pp. 1882–1889, Nov. 2012.

[24] J. Zhang, X. Zhang, and D. Shen, "Design of substrate integrated gap waveguide," in *IEEE MTT-S Int. Microw. Symp. (IMS)*, San Francisco, CA, May 2016, pp. 1–4.

[25] R. J. Cameron, C. Kudsia, and R. Mansour, *Microwave Filters for Communication Systems: Fundamentals, Design, and Applications*. Hoboken, NJ, USA: Wiley, 2007.

[26] M. S. Sorkherizi et al., "Direct-coupled cavity filter in ridge gap waveguide," *IEEE Trans. Compon. Packag. Manuf. Technol.*, vol. 4, no. 3, pp. 490–495, 2014.

[27] S. Birgermajer et al., "Microstrip-ridge gap waveguide filter based on cavity resonators with mushroom inclusions," *IEEE Trans. Microw. Theory Techn.*, vol.66, no.1, pp.136–146, 2018.

[28] Z.-H. Shi et al.,"High-selectivity inverted microstrip gap waveguide bandpass filter using hybrid cavity and stub-loaded ring resonant modes," *IEEE Trans. Circuits Syst. II, Exp. Briefs*, vol. 71, no. 1, pp. 146–150, Jan. 2024.

[29] J.-Y. Deng et al., "Ultracompact bandpass filter based on slow wave substrate integrated groove gap waveguide," *IEEE Trans. Microw. Theory Techn.*, vol. 70, no. 2, pp. 1211–1220, 2022.

[30] N. Huang et al., "Design of dual-band bandpass filter based on 3D printable dual-mode groove gap waveguide," *IEEE MTT-S Int. Microw. Workshop Series on Advanced Materials and Processes for RF and THz Applications (IMWS-AMP)*, pp. 1-3, 2022.

[31] A. Jorge-López et al., "Theoretical and experimental results for multipactor effect in groove gap waveguide bandpass filters with inductive coupling irises," *IEEE Access*, pp. 187844–187856, 2024.

[32] Z. Shi et al., "Performance analysis of PPM-SNSPD system for deep space optical communications," *IEEE Transactions on Communications*, vol. 73, no. 8, pp. 6221–6235, Aug. 2025. doi: 10.1109/TCOMM.2025.3529220

[33] W. Tan, et al. "Low-Cost Gap Waveguide Technology Using Shallow Grooves and Glide-Symmetric Semicircular-Holes EBG Structures," IEEE Antennas and Wireless Propagation Letters, vol.22, 2023, pp.2901-2905.

[34] D. Panusch, et al., "A Novel Manufacturing Method for Microwave Components by Lost Wax Casting," IEEE Access, vol.11, 2023, pp.25298-25302.

[35] ECSS-E-HB-20-01A – Multipactor handbook.

[36] M. Malik, et al., "Ku-Band Reflectionless Single- and Dual-Band Bandpass Filters in Groove Gap Waveguide," *IEEE Trans. Microw. Theory Techn.*, vol.83, pp.5813-5827, 2025.

[37] L. Wu, et al., "Design of dual-mode dual-band filter based on multilayer groove gap waveguide," Int. Journal of Electronics and Communications, vol.173, pp.1-6, 2024.